Fast uplift in the Southern Patagonian Andes due to long and short term deglaciation and the asthenospheric window underneath

Veleda A. P. Muller[1], Pietro Sternai[1], Christian Sue[2,3]

[1] Dipartimento di Scienze dell'Ambiente e della Terra (DISAT), Università degli Studi di Milano-Bicocca, Piazza della Scienza 4, Milan, Italy
[2] Institute des Sciences de la Terre (ISTerre), Université Grenoble Alpes, Université Savoie Mont Blanc, CNRS, IRD, IFSTTAR, Université Gustave Eiffel, Grenoble, France.
[3] Université de Franche Comté, Besançon, France.
Correspondence to: Veleda A.P. Muller (v.paivamuller@campus.unimib.it)

Abstract. An asthenospheric window underneath much of the South American continent increases the heat flow in the Southern Patagonian Andes, where glacial-interglacial cycles drive the building and melting of the Patagonian Icefields since the latest Miocene. The Last Glacial Maximum (LGM) was reached ~20000 years ago, and an acceleration of the deglaciation rate is recorded since the Little Ice Age (LIA), ~400 years ago. Fast uplift rates of up to 41±3 mm/yr are measured by GNSS around the Southern Patagonian Icefield and currently ascribed to post-LIA lithospheric rebound, but the possible longer-term post-LGM rebound is poorly constrained. These uplift rates, in addition, are one order of magnitude higher than those measured on other glaciated orogens (e.g., the European Alps), which raises questions about the role of the asthenospheric window in affecting the vertical surface displacement rates. Here, we perform geodynamic thermo-mechanical numerical modelling to estimate the surface uplift rates induced by post-LIA and post-LGM deglaciation accounting for temperature dependent rheologies and different thermal regimes in the asthenosphere. Our modelled maximum postglacial rebound matches the observed uplift rate budget only when both post-LIA and post-LGM deglaciation are accounted for and if a standard continental mantle potential temperature is increased by 150-200 °C. The asthenospheric window thus plays a key role in controlling the magnitude of presently observed uplift rates in the Southern Patagonian Andes.

1 Introduction

Vertical displacements of the Earth's surface with respect to the geoid occur in response to the motion of crustal and mantle rock masses due to plate tectonics and the associated redistribution of sediments, water, and ice by surface processes (e.g., Molnar and England, 1990; Watts, 2001; Champagnac et al., 2012; Sternai, 2023; Cloetingh et al., 2023). For instance, excess of topography in orogenic regions due to convergence and crustal stacking deflects the lithosphere downward, whereas unloading by erosion and ice melting causes upward deflection of the lithosphere, known as "isostatic" adjustment (e.g., Peltier and Andrews, 1976; Peltier, 1996, 2004; Mitrovica and Forte, 1997; Butler and Peltier, 2000; Kaufman and Lambeck, 2002; Watts, 2001; Turcotte and Schubert, 2002). The magnitude of surface uplift rates is set primarily by the lithosphere and asthenosphere viscosities, which depend, amongst other factors, on the thermal field at depth (McKenzie and Richter, 1981; McKenzie and Bickle, 1988; Gurnis, 1989; Ranalli, 1995, 1997; Kaufman et al., 1997; Watts, 2001; Turcotte and Schubert, 2002). Although the theory that relates surface ice load changes and isostatic adjustment is well developed (e.g., Peltier and Andrews, 1976; Peltier, 1996, 2004; Mitrovica and Forte, 1997; Kaufman and Lambeck, 2002; Stuhne and Peltier, 2015; Van der Wal et al., 2015), recognizing and quantifying expressions of such dynamics in natural settings is difficult.

The Southern Patagonian Andes in the South American Continent are located above a transition zone between the subducting Antarctic and Nazca plates and a wide asthenospheric window (Fig. 1a; Cande and Leslie, 1986). The Chile Triple Junction (CTJ) at ~46 °S delimits the surface tip of the asthenospheric window, which opened during the last ~16 Ma from south to north (Ramos and Kay, 1992; Breitsprecher and Thorkelson, 2009). First order effects of the asthenospheric flow on the surface continental geology are the inhibition of arc volcanism in favour of retroarc magmatism, forward propagation of the fold-and-thrust belt, and rock uplift (Ramos and Kay, 1992; Ramos, 2005; Breitsprecher and Thorkelson, 2009; Guillaume et al., 2009; Lagabrielle et al., 2010; Georgieva et al., 2016). Rock uplift due to asthenospheric upwelling, in particular, was estimated as < 0.15 mm/yr in the last 3 Ma over an area of about 100000 km^2 around the CTJ latitude (Guillaume et al., 2009). The heat flow was calculated as >100 mW/m^2 near the CTJ, ~70-90 mW/m^2 in the center of the asthenospheric window (~50 °S), and 50-60 mW/m^2 near its northern boundary (~46 °S) (Ávila and Dávila, 2018), suggesting that the mantle temperature beneath Southern Patagonia is likely higher than in normal subduction zones (Ranalli, 1997).

65   The Patagonian Ice Sheet covered the Southern Patagonian Andes between ~30000

66   and ~17000 years ago, extending from latitudes 38 to 55 °S with estimated area of ~490000

67   km^2 and volume of ~550000 km^3 (Fig. 1 a) based on preserved glacial geomorphologies,

68   stratigraphic and paleoecological records, and geochronological data (Moreno et al., 1999,

69   2005; McCulloch et al., 2000, 2005; Hulton et al., 2002; Rabassa, 2008; Glasser et al., 2005,

70   2016; Glasser and Jansson, 2008; Hein et al., 2010; Boex et al, 2013; Bourgois et al., 2016;

71   Martinod et al., 2016; Bendle et al., 2017; Thorndycraft et al., 2019; Davies et al., 2020). The

72   average and maximum ice thickness were estimated as ~1100 m and ~2500 m, respectively

73   (McCulloch et al., 2000; Hulton et al., 2002; Boex et al., 2013; Davies et al., 2020).

74   Currently, the SPI covers an area of ~13219 km^2 with a volume of 3632 ± 675 km^3, whereas

75   the Northern Patagonian Icefield (NPI) covers an area of ~3976 km^2 with a volume of $1124 \pm$

76   260 km^3 (Fig. 1). The present-day ice thickness reaches up to ~2000 m in deep glacial valleys

77   (Millan et al., 2019). The long term ice loss rate is uncertain, but more than 75% of ice was

78   certainly lost since the Last Glacial Maximum (LGM, approximately 20000 years ago), and

79   some models predicted more than 95% of ice loss with separation between the SPI and NPI in

80   the first 5000 to 10000 years of post-LGM deglaciation (McCulloch et al., 2000; Hulton et

81   al., 2002; Boex et al., 2013; Bourgois et al., 2016; Thorndycraft et al., 2019; Davies et al.,

82   2020).

83   GNSS and remote sensing data show ongoing vertical rock uplift rates between 30 ± 3

84   and 41 ± 3 mm/yr in the northern part of the Southern Patagonian Icefield (SPI, Fig. 1b),

85   gradually decreasing toward its peripheral parts (Aniya, 1996; Aniya et al., 1997; Rignot et

86   al., 2003; Ivins and James, 1999, 2004; Dietrich et al., 2010; Willis et al., 2012; Lange et al.,

87   2014). Such outstandingly high uplift rates are currently ascribed to lithospheric viscoelastic

88   glacial isostatic adjustment (GIA) following the Little Ice Age (LIA), with apex around 1630

89   AD (Ivins and James, 1999, 2004; Glasser et al., 2011). Deglaciation since the LIA was

90   responsible for an ice loss of 503 ± 101.1 km^3 in the SPI (Glasser et al., 2011), with a

91   substantial increase of the glacial recession after the 20th century (Aniya, 1996; Aniya et al.,

92   1997; Rignot et al., 2003; Glasser et al., 2011; Davies and Glasser, 2012; Ivins et al., 2011;

93   Willis et al., 2012). To match the very high observed uplift rate budget, previous GIA studies

94   infer low asthenosphere viscosity (in the order of 10^{18} Pa s) and thin elastic lithosphere (~35

95   km thick) (Ivins and James, 1999, 2004; Klemann et al., 2007; Dietrich et al., 2010; Lange et

96   al, 2014). However, although this is consistent with abnormally high mantle temperatures,

97   viscosity estimates from previous studies are untied to the regional thermal regime, which

3

98   prevents a more thorough characterization of the role of the asthenospheric window

99   underneath the SPI in affecting the observed uplift rates. In addition, the contribution of post-

100 LGM deglaciation to present-day rock uplift rate was marginally addressed. Here, we

101 perform fully coupled thermo-mechanical numerical geodynamic experiments forced by

102 surface unloading scaled on post-LIA and post-LGM ice melting to evaluate their relative

103 contribution to the observed regional uplift rates. Numerical experiments account for a range

104 of positive thermal anomalies in the asthenosphere to further asses the role of the

105 asthenospheric window in setting the mantle viscosity and associated postglacial rebound.

106 Focusing on the magnitude, rather than the pattern, of the inferred surface uplift rates, we use

107 the observed budget of rock uplift rate to constrain plausible thermal and viscosity structures

108 at depth as well as the timing of postglacial rebound.

109

110 **2 Methodology**

111 **2.1 Numerical model**

112 We use a fully coupled thermo-mechanical, visco-elasto-plastic, numerical

113 geodynamic model to quantify the effect of thermal anomalies in the mantle on the magnitude

114 of surface uplift rates due to deglaciation. We provide a short overview of the governing

115 equations hereafter, while a detailed description of numerical technique can be found, for

116 instance, in Gerya and Yuen (2007), Gerya et al. (2019), Sternai (2020), and Muller et al.

117 (2022). The continuity equation allows for the conservation of mass during the displacement

118 of a geological continuum:

119 (1) $\frac{\partial \rho}{\partial t} + \nabla(\rho v) = 0$

120 where ρ is the local density, t is time, v is the velocity vector, and ∇ is the divergence

121 operator. The momentum equation describes the changes in velocity of an object in the

122 gravity field due to internal and external forces:

123 (2) $\frac{\partial \sigma_{ij}}{\partial x_i} + \rho g_i = \rho \left(\frac{\partial v_i}{\partial t} + v_j \frac{\partial v_i}{\partial x_j} \right)$

124 where σ_{ij} is the stress tensor, x_i and x_j are spatial coordinates, and g_i is the i-th component of

125 the gravity vector. The energy equation allows for the conservation of energy during

126 advective and conductive heat transfer in the continuum:

127 (3) $\rho C_P \frac{DT}{Dt} - div(c\nabla T) + v\nabla T = H_r + H_s + H_a + H_l$

128   where P is pressure, T is temperature, C_P is specific heat capacity at a constant P, c is the

129   thermal conductivity, $H_r + H_s + H_a + H_l$ are the volumetric heat productions by

130   radiogenic, shear, adiabatic and latent heat, respectively. $H_a \propto \frac{DP}{Dt}$, $H_s = \sigma'_{ij}\dot{\varepsilon}'_{ij(viscous)}$, and

131   H_r and H_l are the radiogenic and latent heat productions.

132   Ductile deformation is thermally activated generating viscous flow, which involves

133   diffusion and dislocation creep, calculated according to the material shear viscosity:

134   (4) $\frac{1}{\eta_{ductile}} = \frac{1}{\eta_{diff}} + \frac{1}{\eta_{disl}}$

135   with

136        $\eta_{diff} = \frac{\eta_0}{2\sigma_{cr}^{n-1}} exp\left(\frac{E_a + PV_a}{RT}\right)$, and

137        $\eta_{disl} = \frac{\eta_0^{\frac{1}{n}}}{2} exp\left(\frac{E_a + PV_a}{nRT}\right) \dot{\varepsilon}_{II}^{\frac{1}{n}-1}$

138   where η_{diff} and η_{disl} are the shear viscosity for diffusion and dislocation creep, respectively,

139   η_0 is the material static viscosity, σ_{cr} is the diffusion-dislocation transition critical stress, n is

140   the stress exponent, E_a is the activation energy, V_a is the activation volume, R is the gas

141   constant, and $\dot{\varepsilon}_{II}$ is the second invariant of the strain rate tensor. The viscous deviatoric strain

142   rate tensor, $\dot{\varepsilon}'_{ij (viscous)}$, is defined by:

143   (5) $\dot{\varepsilon}'_{ij (viscous)} = \frac{1}{2\eta_{ductile}}\sigma'_{ij} + \delta_{ij}\eta_{bulk}\dot{\varepsilon}_{kk} = \frac{1}{2\eta_{diff}}\sigma'_{ij} + \frac{1}{2\eta_{disl}}\sigma'_{ij} + \delta_{ij}\eta_{bulk}\dot{\varepsilon}_{kk}$

144   where σ'_{ij} is the deviatoric stress tensor, δ_{ij} is the Kronecker delta, $\dot{\varepsilon}_{kk}$ is the volumetric

145   strain rate (e.g., related to phase transformations), and η_{bulk} is the bulk viscosity.

146   Recoverable deformation is defined by the elastic deviatoric strain rate tensor, $\dot{\varepsilon}'_{ij (elastic)}$, as:

147   (6) $\dot{\varepsilon}'_{ij (elastic)} = \frac{1}{2\mu} \frac{\breve{D}\sigma'_{ij}}{Dt}$

148   where μ is the shear modulus and $\frac{\breve{D}\sigma'_{ij}}{Dt}$ is the objective co-rotational time derivative of the

149   deviatoric stress tensor. The plastic deformation, brittle and localised, occurs at low

150   temperature when the absolute shear stress limit, σ_{yield}, is reached, with

151   (7) $\sigma_{yield} = C + \sin(\varphi)P$

152   where C is cohesion and φ is the effective internal friction angle. The plastic strain rate

153   tensor, $\dot{\varepsilon}'_{ij (plastic)}$, is defined as:

154   (8) $\dot{\varepsilon}'_{ij (plastic)} = 0 \; for \; \sigma_{II} < \sigma_{yield}, \; \dot{\varepsilon}'_{ij (plastic)} = \mathcal{X}\frac{\partial\sigma'_{ij}}{2\sigma_{II}} \; for \; \sigma_{II} \geq \sigma_{yield}$

155   where $\mathcal{X}$ is the plastic multiplier which satisfies the plastic yielding condition $\sigma_{II} = \sigma_{yield}$.

156   The bulk strain rate tensor, $\dot{\varepsilon}'_{ij(bulk)}$, integrates the viscous, elastic and plastic deformation:

157   (9) $\dot{\varepsilon}'_{ij(bulk)} = \dot{\varepsilon}'_{ij(viscous)} + \dot{\varepsilon}'_{ij(elastic)} + \dot{\varepsilon}'_{ij(plastic)}$

158   **2.2 Reference model setup and modeling approach**

159   The model domain, scaled on the study region, is 700 km wide and 120 km thick.
160   From top to bottom, the model accounts for 10 km of 'sticky' air, 30 km of continental crust
161   (with rheology of quartzite, Ranalli, 1995), 30 km of lithospheric mantle, and 50 km of
162   asthenospheric mantle (with rheology of dry dunite, Ranalli, 1995), in agreement with
163   literature data (e.g., Klemann et al., 2007). The initial geotherm is piece-wise linear resulting
164   from an adiabatic temperature gradient of 0.5 °C/km in the asthenosphere (Turcotte and
165   Schubert, 2002) and thermal boundary conditions equal to 0 °C at the surface and 1327 °C at
166   the bottom of the lithosphere, with nil horizontal heat flux across the vertical boundaries. The
167   rheologic and thermal structure of the reference model give a lithospheric elastic thickness,
168   *Te* (*sensu* Burov and Diament, 1995), of ~30 km, comparable to previous estimates
169   underneath the SPI based on GIA models (Ivins and James, 1999; Dietrich et al., 2010; Lange
170   et al., 2014), heat flow data (Ávila and Dávila, 2018), and waveform inversion (Robertson
171   Maurice et al., 2003). Rocks rheological properties are listed in Table 1.

172   The numerical model uses the finite differences with marker-in-cell technique,
173   resolved by 51 × 61 nodes in x and y directions, respectively, distributed on a Eulerian grid
174   that accounts for a maximum resolution of 1 km along the y direction in the upper part of the
175   model domain, and ~13 km in the x direction. 400 × 400 Lagrangian markers are randomly
176   distributed along the x and y dimensions and used for advecting the material properties
177   (Gerya and Yuen, 2007; Gerya et al., 2019). The material properties carried by Lagrangian
178   markers are then interpolated onto the Eulerian grid via a 4th order Runge-Kutta interpolation
179   scheme. An internal free surface is simulated through the 10 km thick layer of sticky air. The
180   velocity boundary conditions are free slip at all boundaries (x = 0 and x = 700 km; y = 0 and
181   y = 120 km).

182   On the top of the crust and in the middle of the model domain we impose a 2 km thick
183   pseudo-icecap to simulate lithospheric unloading during deglaciation. The pseudo-icecap is
184   70 km wide for the post-LIA model set and 200 km wide for the post-LGM model sets (Fig. 2
185   a). We compute the surface load, *L*, as

186   (10) $L = \rho_{ice} g h_{ice}$,

187   where ρ_{ice} is the pseudo-icecap density, *g* is the gravity acceleration, and h_{ice} is the pseudo-
188   icecap thickness, and deglaciation occurs by gradually reducing h_{ice} in time (Fig. 2 b, c). We
189   run two sets of experiments for the post-LGM deglaciation. In *Model set 1,* 75% of ice loss

190 occurs in 20000 years (i.e., 1500 m drop of ice thickness, Fig. 2 b), thus assuming a

191 conservative estimate of ice loss since the beginning of the LGM until the present-day. In

192 *Model set 2*, 95% of ice loss occurs in 10000 years (i.e., 1900 m drop of ice thickness, Fig. 2

193 b), assuming faster deglaciation rates of the Patagonian Ice Sheet in the first half of post-

194 LGM deglaciation (McCulloch et al., 2000; Hulton et al., 2002; Boex et al., 2013; Bendle et

195 al., 2017; Thorndycraft et al., 2019; Davies et al., 2020). For the post-LIA deglaciation, we

196 simulate 10% of ice loss in 400 years (i.e., 200 m drop of ice thickness, Fig. 2 c) (Aniya,

197 1996; Aniya et al., 1997; Rignot et al., 2003; Ivins and James, 1999, 2004; Dietrich et al.,

198 2010; Willis et al., 2012; Lange et al., 2014).

199 In the models the initial lateral extent of the pseudo-icecap does not change

200 throughout the deglaciation. Although this simplification may affect the inferred pattern of

201 postglacial rebound, it greatly facilitates the simulation of deglacial lithospheric unloading

202 without significantly affecting the magnitude of postglacial rebound, which is the main focus

203 here. All simulations account for some spin up time before the deglaciation begins, so that the

204 lithosphere-asthenosphere system adjusts to the pseudo-icecap initial load. The surface uplift

205 rate during the deglaciation is calculated through time as the surface elevation change

206 resulting from the modelled strain field divided by the viscoelastic timestep. Given the

207 geologically short time window investigated here, we neglect deformation related to longer

208 term tectonic forces. The parametric study focuses on the mantle potential temperature (*sensu*

209 McKenzie and Bickle, 1988) which accounts for positive thermal anomalies, TA, of up to

210 200 °C in steps of 50 ° C, added to the reference mantle potential temperature of 1265 °C

211 (McKenzie and Bickle, 1988; Currie and Hyndman, 2006; Ávila and Dávila, 2018; Sternai,

212 2020) to mimic the presence of a slab window at depth.

3 Results

Results are shown in Table 2 and Figs. 4-7. In agreement with the theory of lithospheric flexure (e.g., Turcotte and Schubert, 2002) the deglaciation triggers uplift in the region covered by the melting pseudo-icecap and subsidence in the neighbouring regions (Figs. 4-6). Overall, increasing the mantle potential temperature decreases the asthenospheric viscosity, with significant effects on the magnitude of the modelled surface velocity field. The asthenosphere viscosity ranges between 10^{22}-10^{19} Pa s in simulations with TA equal to 0 (reference model), 50 and 100 °C, and between 10^{19}-10^{16} Pa s in simulations with TA equal to 150 and 200 °C (Fig. 3 a-d). Lithospheric warming due to increasing mantle potential temperature also leads to a reduction of the lower lithosphere viscosity (from 10^{22} to 10^{20} Pa s), thereby decreasing the integrated lithospheric strength.

In *Model set 1* for Post-LGM deglaciation, when TA is 0 (reference model) the maximum uplift rates is < 1 mm/yr during the first 5000 years of the deglaciation, increasing gradually up to 9.5 mm/yr in the later stages of the deglaciation (i.e., 20000 years, Fig. 4). When TA equals 50, 100, 150 and 200 °C, the maximum uplift rates can reach up to ~2, ~5, ~12, and ~15 mm/yr, respectively, already in the first 1000 years of the deglaciation (Fig. 4 a). When TA is 50 and 100 °C the maximum uplift rate is subject to a protracted increase in time, reaching up to ~12 and ~14 mm/yr after 20000 years of deglaciation (Figs. 4 b-d and 7 a). For TA equal to 150 and 200 °C, the maximum uplift rate reach a plateau between 11 and 17 mm/yr during the 20000 years of deglaciation (Figs. 4 and 7 a, Table 2). After the end of the deglaciation, the maximum uplift rate takes longer than about 5000 years to re-equilibrate to 0 mm/yr when TA ≤ 100 °C, whereas it drops to 0 mm/yr almost immediately when TA is 150 or 200 °C (Fig. 7 a).

In the *Model set 2* for Post-LGM deglaciation, the maximum uplift rate is less than 2 mm/yr during the first 1000 years of deglaciation when TA is 0, 50 and 100 °C, whereas it reaches up to ~22 and ~30 mm/yr during in the first 1000 years of deglaciation when TA is 150 and 200 °C (Fig. 5 a, 7 b, and Table 2). Between 5000 and 10000 years of deglaciation, the maximum uplift rate increases to ~19, ~25 and ~36 mm/yr, respectively when TA is 0, 50 and 100 °C, whereas it reach up to between 36 and 41 mm/yr between 50000 and 1000 years of deglaciation when TA equal to 150 and 200 °C. The maximum uplift rate decreases slower if TA is 0, 50 and 100 °C, taking longer than 5000 year after the deglaciation to drop to values <5 mm/yr (Fig. 7 b and Table 2), whereas it quickly drops to < 2 mm/yr when the deglaciation is over and TA is 150 and 200°C (Figs. 5 b-d and 7b). Overall, a warmer and

246   less viscous asthenosphere generates a higher magnitude and fast changing postglacial
247   rebound than a cooler and more viscous asthenosphere.

248   In the post-LIA model set, the maximum uplift rate is ~1.4, ~2.3 and ~2.2 mm/yr
249   during the first 100 years of deglaciation when TA is respectively 0, 50, and 100 °C, whereas
250   it reaches ~8.3 and ~23 mm/yr during the same interval when TA is respectively 150 and 200
251   °C (Figs. 6 a, 7 c, and Table 2). Between 200 and 400 years of deglaciation, the maximum
252   uplift rate reaches ~1.9, ~2.5 and ~3 mm/yr when TA equal to 0, 50 and 100 °C, and ~14 and
253   ~25.5 mm/yr when TA is 150 and 200 °C, respectively (Figs. 6 c-d, 7 c, and Table 2). When
254   the deglaciation ends, the maximum uplift rate drops to ~0 mm/yr in ~ 100 years when TA ≤
255   100 °C, whereas it takes longer than 1000 years when TA equals 150 °C or 200 °C (Fig. 7 c).
256   Overall, a warmer and less viscous asthenosphere generates a higher magnitude postglacial
257   rebound which, however, takes much longer to re-equilibrate to 0 mm/yr after the end of the
258   deglaciation than a cooler and more viscous asthenosphere.
259

260   **4 Discussion and conclusions**

261   Our modelling is simplistic in that we impose a linear and uniform ice loss instead of
262   a more realistic ice-sheet melting pattern in space and time. This choice is motivated by the
263   limited data reporting on the SPI melting velocities and associated redistribution of the
264   surface masses, which cover time spans much shorter than the post-LIA and post-LGM time
265   windows investigated here (Aniya, 1996; Aniya et al., 1997; Rignot et al., 2003; Ivins and
266   James, 1999, 2004; Willis et al., 2012; Dietrich et al., 2010; Lange et al., 2014). As
267   previously highlighted (Hulton et al., 2002; Rabassa, 2008; Glasser et al., 2011; Davis and
268   Glasser, 2012; Martinod et al., 2016; Bendle et al., 2017; Davies et al., 2020), constraints
269   regarding the ice-sheet mass balance and melting velocities throughout the time windows of
270   interest are difficult to obtain from the preserved geomorphological, stratigraphic and
271   geochronological records. We also assume a homogeneous lithosphere and neglect lateral
272   viscosity variations in the asthenosphere (Klemann et al., 2007) despite the long-term
273   southern Andean orogenic history (Cande and Leslie, 1986; Ramos, 2005; Muller et al.,
274   2021). Notwithstanding these limitations, however, our fully coupled numerical thermo-
275   mechanical geodynamic models provide realistic uplift rates that one can compare to current
276   geodetic observations. Following the example of previous studies (Ivins and James, 1999,
277   2004; Klemann et al., 2007; Dietrich et al., 2010; Lange et al., 2014), we discuss our results
278   assuming that GNSS-measured rock uplift rates are mostly related to the deglaciation history

279 and only marginally controlled by the longer term geodynamics (e.g., Ramos, 2005; Muller et

280 al., 2021).

281 We first remark that inferred maximum post-LIA uplift rate of up to a few mm/yr

282 from experiments without or with a low asthenospheric thermal anomaly (TA ≤ 100 °C) are

283 within the same order of magnitude of maximum uplift rates measured in collisional orogens

284 such as the European Alps (Sue et al., 2007; Serpelloni et al., 2013; Walpersdorf et al., 2015;

285 Sternai et al., 2019) and the Himalayas (Larson et al., 1999). Since these collisional orogens

286 are characterized by a thicker lithosphere (Geissler et al., 2010; Ravikumar et al., 2020), they

287 are likely less sensitive to mantle dynamics than the Southern Patagonian Andes. When we

288 consider lithospheric unloading due to post-LGM deglaciation of a wider ice sheet, however,

289 the inferred maximum uplift rate via *Model set 1* and *Model set 2* reaches up to 10 mm/yr for

290 and 20 mm/yr, respectively, even without asthenospheric thermal anomaly. This suggests a

291 that a contribution from long-term postglacial rebound to the present-day uplift rates

292 measured in the SPI is likely.

293 In the Southern Patagonian Andes, the regional asthenosphere viscosity was estimated

294 between 1.6 and 8×10^{18} Pa s from GIA models based on GNSS and satellite observations

295 (Ivins and James, 1999, 2004; Klemann et al., 2007; Dietrich et al., 2010; Willis et al., 2012;

296 Lange et al., 2014). Similarly, the asthenosphere viscosity from our models when TA > 100

297 °C is < 10^{19} Pa s, with the lowest viscosity value of 10^{16} Pa s imposed where partial melting,

298 supported by the regional Holocene volcanism (Stern and Kilian, 1996), occurs. Under these

299 conditions, however, our experiments provide uplift rates between 14 and 26 mm/yr for post-

300 LIA deglaciation indicating that, even with a very low viscosity asthenosphere, the rebound

301 due to the short-term post-LIA deglaciation does not reach the presently observed maximum

302 uplift rates of 41 ± 3 mm/yr. Experiments that account for a low viscosity asthenosphere and

303 long-term post-LGM deglaciation lasting for 20000 years and 10000 years reach up to ~25

304 and ~42 mm/yr of uplift rate, respectively, comparable to present-day values. Results,

305 therefore, indicate that the outstanding observational budget of rock uplift in the SPI is

306 matched only when accounting for higher-than-normal mantle temperatures, thereby

307 highlighting the relevance of the regional asthenospheric window.

308 Because of the limited knowledge regarding the timing and amount of ice loss since

309 the LGM (e.g., Davies et al., 2020), it is difficult to position in time present-day uplift rate

310 measurements within the investigated deglaciation scenarios to assess the contribution of

311 post-LGM and post-LIA deglaciation to the maximum uplift rate budget. In the faster post-

312 LGM deglaciation scenario (*Model set 2*) the observed maximum uplift rate budget is

313   attained in about 10000 years of deglaciation, but only minor residual rebound could be

314   observed today regardless of the amount of ice loss (Fig. 7 b). If post-LGM deglaciation

315   occurred slower (*Model set 1*), this event may contribute to up to 40% to the present-day

316   uplift rate budget. Although it is difficult to reconcile this scenario with the geomorphological

317   and geochronological evidences (Hulton et al., 2002; Boex et al., 2013; Davis and Glasser,

318   2012; Martinod et al., 2016; Bendle et al., 2017; Thorndycraft et al., 2019; Davies et al.,

319   2020), it appears that post-LIA rebound alone cannot cover the entire budget of the observed

320   uplift rates even with the highest tested TA, which points to a non-negligible contribution

321   from post-LGM deglaciation. This latter conclusion is reinforced by estimates of the mantle

322   relaxation time, τ_r, as (Turcotte and Schubert, 2002):

323   (11) $\tau_r = \frac{4\pi v}{g\lambda}$,

324   where v is the asthenosphere viscosity, λ is the width of the ice sheet, and g is the

325   gravity acceleration. Using $10^{16} < v < 10^{18}$ Pa s and $\lambda = 200$ km leads to $\sim 2000 < \tau_r < \sim 200000$

326   years, a time range considerably longer than the post-LIA deglaciation and including full

327   Pleistocene glacial-interglacial cycles (Ruddiman et al., 1986). We therefore propose that

328   currently observed uplift rates in the Southern Andes are driven by both post-LGM and post

329   LIA lithospheric rebound enhanced by a thermal anomaly of at least 150 °C due to the

330   regional asthenospheric window which lowers mantle viscosities.

331   As a final consideration, our models suggest that we shall measure regional uplift

332   rates in the order of the tens of cm/yr in the next century if the currently observed ice loss rate

333   of at least -20 Gt/yr in the SPI (Willis et al., 2012) will continue until the total meltdown of

334   the ice sheet in ~200 years.

335

336   **5 Acknowledgements**

337

343

344 **References**

345 Aniya, M. (1996). Holocene variations of Ameghino glacier, southern Patagonia. *The*
346 *Holocene*, *6*(2), 247-252.

347 Aniya, M., Sato, H., Naruse, R., Skvarca, P., & Casassa, G. (1997). Recent glacier variations
348 in the Southern Patagonia icefield, South America. *Arctic and Alpine Research*, *29*(1), 1-12.

349 Ávila, P., & Dávila, F. M. (2018). Heat flow and lithospheric thickness analysis in the
350 Patagonian asthenospheric windows, southern South America. *Tectonophysics*, *747*, 99-107.

351 Bendle, J. M., Palmer, A. P., Thorndycraft, V. R., & Matthews, I. P. (2017). High-resolution
352 chronology for deglaciation of the Patagonian Ice Sheet at Lago Buenos Aires (46.5 S)
353 revealed through varve chronology and Bayesian age modelling. *Quaternary Science*
354 *Reviews*, *177*, 314-339.

355 Boex, J., Fogwill, C., Harrison, S., Glasser, N. F., Hein, A., Schnabel, C., & Xu, S. (2013).
356 Rapid thinning of the late Pleistocene Patagonian Ice Sheet followed migration of the
357 Southern Westerlies. *Scientific Reports*, *3*(1), 1-6.

358 Bourgois, J., Cisternas, M. E., Braucher, R., Bourlès, D., & Frutos, J. (2016). Geomorphic
359 records along the general Carrera (Chile)–Buenos Aires (Argentina) glacial lake (46–48 S),
360 climate inferences, and glacial rebound for the past 7–9 ka. *The Journal of Geology*, *124*(1),
361 27-53.

362 Breitsprecher, K., & Thorkelson, D. J. (2009). Neogene kinematic history of Nazca–
363 Antarctic–Phoenix slab windows beneath Patagonia and the Antarctic Peninsula.
364 *Tectonophysics*, *464*(1-4), 10-20.

365 Burov, E. B., & Diament, M. (1995). The effective elastic thickness (T e) of continental
366 lithosphere: What does it really mean?. *Journal of Geophysical Research: Solid Earth*,
367 *100*(B3), 3905-3927.

368 Butler, S. L., & Peltier, W. R. (2000). On scaling relations in time-dependent mantle
369 convection and the heat transfer constraint on layering. *Journal of Geophysical Research:*
370 *Solid Earth*, *105*(B2), 3175-3208.

371 Cande, S. C., & Leslie, R. B. (1986). Late Cenozoic tectonics of the southern Chile trench.
372 *Journal of Geophysical Research: Solid Earth*, *91*(B1), 471-496.

373 Champagnac, J. D., Molnar, P., Sue, C., & Herman, F. (2012). Tectonics, climate, and
374 mountain topography. *Journal of Geophysical Research: Solid Earth*, *117*(B2).

375 Cloetingh, S., Sternai, P., Koptev, A., Ehlers, T. A., Gerya, T., Kovács, I., Oerlemans, J.,
376 Beekman, F., Lavallée, Y., Dingwell, D., Békési, E., Porkolàb, K., Tesauro, M., Lavecchia,
377 A., Botsyun, S., Muller, V., Roure, F., Serpelloni, E., Matenco, L., Castelltort, S.,
378 Giovannelli, D., Brovarone, A.V., Malaspina, N., Coletti, G., Valla, P., & Limberger, J.
379 (2023). Coupled surface to deep Earth processes: Perspectives from TOPO-EUROPE with an
380 emphasis on climate-and energy-related societal challenges. *Global and Planetary Change*,
381 104140.

382 Currie, C. A., & Hyndman, R. D. (2006). The thermal structure of subduction zone back arcs.
383 *Journal of Geophysical Research: Solid Earth*, *111*(B8).

384 Davies, B. J., & Glasser, N. F. (2012). Accelerating shrinkage of Patagonian glaciers from the
385 Little Ice Age (~ AD 1870) to 2011. *Journal of Glaciology*, *58*(212), 1063-1084.

386 Davies, B. J., Darvill, C. M., Lovell, H., Bendle, J. M., Dowdeswell, J. A., Fabel, D., García,

387 J.-L., Geiger, A., Glasser, N.F., Gheorghiu, D.M., Harrison, S., Hein, A.S., Kaplan, M.R.,
388 Martin, J.R.V., Mendelova, M., Palmer, A., Pelto, M., Rodés, A., Segredo, E.A., Smedley,
389 R.K., Smellie J., & Thorndycraft, V. R. (2020). The evolution of the Patagonian Ice Sheet
390 from 35 ka to the present day (PATICE). *Earth-Science Reviews*, *204*, 103152.

391 Dietrich, R., Ivins, E. R., Casassa, G., Lange, H., Wendt, J., & Fritsche, M. (2010). Rapid
392 crustal uplift in Patagonia due to enhanced ice loss. *Earth and Planetary Science Letters*,
393 *289*(1-2), 22-29.

394 Geissler, W. H., Sodoudi, F., & Kind, R. (2010). Thickness of the central and eastern
395 European lithosphere as seen by S receiver functions. *Geophysical Journal International*,
396 *181*(2), 604-634.

397 Georgieva, V., Melnick, D., Schildgen, T. F., Ehlers, T. A., Lagabrielle, Y., Enkelmann, E.,
398 & Strecker, M. R. (2016). Tectonic control on rock uplift, exhumation, and topography above
399 an oceanic ridge collision: Southern Patagonian Andes (47 S), Chile. *Tectonics*, *35*(6), 1317-
400 1341.

401 Gerya, T. (2019). *Introduction to numerical geodynamic modelling*. Cambridge University
402 Press.

403 Gerya, T. V., & Yuen, D. A. (2007). Robust characteristics method for modelling multiphase
404 visco-elasto-plastic thermo-mechanical problems. *Physics of the Earth and Planetary*
405 *Interiors*, *163*(1-4), 83-105.

406 Glasser, N. F., Harrison, S., Jansson, K. N., Anderson, K., & Cowley, A. (2011). Global sea-
407 level contribution from the Patagonian Icefields since the Little Ice Age maximum. *Nature*
408 *Geoscience*, *4*(5), 303-307.

409 Glasser, N. F., Jansson, K. N., Harrison, S., & Rivera, A. (2005). Geomorphological evidence
410 for variations of the North Patagonian Icefield during the Holocene. *Geomorphology*, *71*(3-
411 4), 263-277.

412 Glasser, N., & Jansson, K. (2008). The glacial map of southern South America. *Journal of*
413 *Maps*, *4*(1), 175-196.

414 Glasser, N. F., Jansson, K. N., Duller, G. A., Singarayer, J., Holloway, M., & Harrison, S.
415 (2016). Glacial lake drainage in Patagonia (13-8 kyr) and response of the adjacent Pacific
416 Ocean. *Scientific reports*, *6*(1), 21064.

417 Guillaume, B., Martinod, J., Husson, L., Roddaz, M., & Riquelme, R. (2009). Neogene uplift
418 of central eastern Patagonia: dynamic response to active spreading ridge subduction?.
419 *Tectonics*, *28*(2).

420 Gurnis, M. (1989). A reassessment of the heat transport by variable viscosity convection with
421 plates and lids. *Geophysical Research Letters*, *16*(2), 179-182.

422 Hein, A. S., Hulton, N. R., Dunai, T. J., Sugden, D. E., Kaplan, M. R., & Xu, S. (2010). The
423 chronology of the Last Glacial Maximum and deglacial events in central Argentine
424 Patagonia. *Quaternary Science Reviews*, *29*(9-10), 1212-1227.

425 Hirschmann, M. M. (2000). Mantle solidus: Experimental constraints and the effects of
426 peridotite composition. *Geochemistry, Geophysics, Geosystems*, *1*(10).

427 Hulton, N. R., Purves, R. S., McCulloch, R. D., Sugden, D. E., & Bentley, M. J. (2002). The
428 last glacial maximum and deglaciation in southern South America. *Quaternary Science*
429 *Reviews*, *21*(1-3), 233-241.

430 Ivins, E. R., & James, T. S. (1999). Simple models for late Holocene and present-day

431   Patagonian glacier fluctuations and predictions of a geodetically detectable isostatic response.
432   *Geophysical Journal International*, *138*(3), 601-624.

433   Ivins, E. R., & James, T. S. (2004). Bedrock response to Llanquihue Holocene and present-
434   day glaciation in southernmost South America. *Geophysical Research Letters*, *31*(24).

435   Ivins, E. R., Watkins, M. M., Yuan, D. N., Dietrich, R., Casassa, G., & Rülke, A. (2011). On-
436   land ice loss and glacial isostatic adjustment at the Drake Passage: 2003–2009. *Journal of*
437   *Geophysical Research: Solid Earth*, *116*(B2).

438   Johannes, W. (1985). The significance of experimental studies for the formation of
439   migmatites. In: *Migmatites*, Ed. Ashworth, J. R. Blackie & Son Ltd, USA Chapman & Hall.

440   Kaufmann, G., & Lambeck, K. (2002). Glacial isostatic adjustment and the radial viscosity
441   profile from inverse modeling. *Journal of Geophysical Research: Solid Earth*, *107*(B11),
442   ETG-5.

443   Kaufmann, G., Wu, P., & Wolf, D. (1997). Some effects of lateral heterogeneities in the
444   upper mantle on postglacial land uplift close to continental margins. Geophysical Journal
445   International, 128(1), 175-187.

446   Klemann, V., Ivins, E. R., Martinec, Z., & Wolf, D. (2007). Models of active glacial isostasy
447   roofing warm subduction: Case of the South Patagonian Ice Field. *Journal of Geophysical*
448   *Research: Solid Earth*, *112*(B9).

449   Lagabrielle, Y., Scalabrino, B., Suarez, M., & Ritz, J. F. (2010). Mio-Pliocene glaciations of
450   Central Patagonia: New evidence and tectonic implications. *Andean Geology*, *37*(2), 276-299.

451   Lange, H., Casassa, G., Ivins, E. R., Schröder, L., Fritsche, M., Richter, A., Groh, A., &
452   Dietrich, R. (2014). Observed crustal uplift near the Southern Patagonian Icefield constrains
453   improved viscoelastic Earth models. *Geophysical Research Letters*, *41*(3), 805-812.

454   Larson, K. M., Bürgmann, R., Bilham, R., & Freymueller, J. T. (1999). Kinematics of the
455   India-Eurasia collision zone from GPS measurements. *Journal of Geophysical Research:*
456   *Solid Earth*, *104*(B1), 1077-1093.

457   Martinod, J., Pouyaud, B., Carretier, S., Guillaume, B., & Hérail, G. (2016). Geomorphic
458   Records along the General Carrera (Chile)–Buenos Aires (Argentina) Glacial Lake (46°–48°
459   S), Climate Inferences, and Glacial Rebound for the Past 7–9 ka: A discussion. The Journal
460   of Geology, 124(5), 631-635.

461   McCulloch, R. D., Bentley, M. J., Purves, R. S., Hulton, N. R., Sugden, D. E., & Clapperton,
462   C. M. (2000). Climatic inferences from glacial and palaeoecological evidence at the last
463   glacial termination, southern South America. *Journal of Quaternary Science: Published for*
464   *the Quaternary Research Association*, *15*(4), 409-417.

465   McCulloch, R. D., Fogwill, C. J., Sugden, D. E., Bentley, M. J., & Kubik, P. W. (2005).
466   Chronology of the last glaciation in central Strait of Magellan and Bahía Inútil, southernmost
467   South America. *Geografiska Annaler: Series A, Physical Geography*, *87*(2), 289-312.

468   Mckenzie, D. A. N., & Bickle, M. J. (1988). The volume and composition of melt generated
469   by extension of the lithosphere. *Journal of petrology*, *29*(3), 625-679.

470   McKenzie, D., & Richter, F. M. (1981). Parameterized thermal convection in a layered region
471   and the thermal history of the Earth. *Journal of Geophysical Research: Solid Earth*, *86*(B12),
472   11667-11680.

473   Moreno, P. I., Lowell, T. V., Jacobson Jr, G. L., & Denton, G. H. (1999). Abrupt vegetation

474   and climate changes during the last glacial maximum and last termination in the Chilean Lake
475   District: a case study from Canal de la Puntilla (41 S). Geografiska Annaler: Series A,
476   Physical Geography, 81(2), 285-311.

477   Millan, R., Rignot, E., Rivera, A., Martineau, V., Mouginot, J., Zamora, R., Uribe, J.,
478   Lenzano, G., De Fleurian, B., Li, X., Gim, Y., & Kirchner, D. (2019). Ice thickness and bed
479   elevation of the Northern and Southern Patagonian Icefields. *Geophysical Research Letters*,
480   *46*(12), 6626-6635.

481   Mitrovica, J. X., & Forte, A. M. (1997). Radial profile of mantle viscosity: Results from the
482   joint inversion of convection and postglacial rebound observables. *Journal of Geophysical
483   Research: Solid Earth*, *102*(B2), 2751-2769.

484   Molnar, P., & England, P. (1990). Late Cenozoic uplift of mountain ranges and global
485   climate change: chicken or egg? *Nature*, *346*(6279), 29-34.

486   Moreno, P. I., Denton, G. H., Moreno, H., Lowell, T. V., Putnam, A. E., & Kaplan, M. R.
487   (2015). Radiocarbon chronology of the last glacial maximum and its termination in
488   northwestern Patagonia. *Quaternary Science Reviews*, *122*, 233-249.

489   Muller, V. A., Calderón, M., Fosdick, J. C., Ghiglione, M. C., Cury, L. F., Massonne, H. J.,
490   Fanning, M.C., Warren, C.J., Ramírez de Arellano, C., & Sternai, P. (2021). The closure of
491   the Rocas Verdes Basin and early tectono-metamorphic evolution of the Magallanes Fold-
492   and-Thrust Belt, southern Patagonian Andes (52–54° S). *Tectonophysics*, *798*, 228686.

493   Muller, V. A., Sternai, P., Sue, C., Simon-Labric, T., & Valla, P. G. (2022). Climatic control
494   on the location of continental volcanic arcs. *Scientific Reports*, *12*(1), 1-13.

495   Peltier, W. R. (1996). Mantle viscosity and ice-age ice sheet topography. *Science*, *273*(5280),
496   1359-1364.

497   Peltier, W. R. (2004). Global glacial isostasy and the surface of the ice-age Earth: the ICE-5G
498   (VM2) model and GRACE. *Annu. Rev. Earth Planet. Sci.*, *32*, 111-149.

499   Peltier, W. R., & Andrews, J. T. (1976). Glacial-isostatic adjustment—I. The forward
500   problem. *Geophysical Journal International*, *46*(3), 605-646.

501   Rabassa, J. (2008). Late cenozoic glaciations in Patagonia and Tierra del Fuego.
502   *Developments in quaternary sciences*, *11*, 151-204.

503   Ramos, V. A. (2005). Seismic ridge subduction and topography: Foreland deformation in the
504   Patagonian Andes. *Tectonophysics*, *399*(1-4), 73-86.

505   Ramos, V. A., & Kay, S. M. (1992). Southern Patagonian plateau basalts and deformation:
506   backarc testimony of ridge collisions. *Tectonophysics*, *205*(1-3), 261-282.

507   Ranalli, G. (1995). *Rheology of the Earth*. Springer Science & Business Media.

508   Ranalli, G. (1997). Rheology of the lithosphere in space and time. *Geological Society,
509   London, Special Publications*, *121*(1), 19-37.

510   Ravikumar, M., Singh, B., Pavan Kumar, V., Satyakumar, A. V., Ramesh, D. S., & Tiwari,
511   V. M. (2020). Lithospheric density structure and effective elastic thickness beneath Himalaya
512   and Tibetan Plateau: Inference from the integrated analysis of gravity, geoid, and topographic
513   data incorporating seismic constraints. *Tectonics*, *39*(10), e2020TC006219.

514   Rignot, E., Rivera, A., & Casassa, G. (2003). Contribution of the Patagonia Icefields of South
515   America to sea level rise. *Science*, *302*(5644), 434-437.

516   Robertson Maurice, S. D., Wiens, D. A., Koper, K. D., & Vera, E. (2003). Crustal and upper

517 mantle structure of southernmost South America inferred from regional waveform inversion.
518 *Journal of Geophysical Research: Solid Earth*, *108*(B1).

519 Ruddiman, W. F., Raymo, M., & McIntyre, A. (1986). Matuyama 41,000-year cycles: North
520 Atlantic Ocean and northern hemisphere ice sheets. *Earth and Planetary Science Letters*,
521 *80*(1-2), 117-129.

522 Serpelloni, E., Faccenna, C., Spada, G., Dong, D., & Williams, S. D. (2013). Vertical GPS
523 ground motion rates in the Euro-Mediterranean region: New evidence of velocity gradients at
524 different spatial scales along the Nubia-Eurasia plate boundary. *Journal of Geophysical*
525 *Research: Solid Earth*, *118*(11), 6003-6024.

526 Stern, C. R., & Kilian, R. (1996). Role of the subducted slab, mantle wedge and continental
527 crust in the generation of adakites from the Andean Austral Volcanic Zone. Contributions to
528 mineralogy and petrology, 123, 263-281.

529 Sternai, P. (2020). Surface processes forcing on extensional rock melting. *Scientific reports*,
530 *10*(1), 1-13.

531 Sternai, P. (2023). Feedbacks between internal and external Earth dynamics. In *Dynamics of*
532 *Plate Tectonics and Mantle Convection* (pp. 271-294). Elsevier.

533 Sternai, P., Sue, C., Husson, L., Serpelloni, E., Becker, T. W., Willett, S. D., Faccenna, C., Di
534 Giulio, A., Spada, G., Jolivet, L., Valla, P., Petit, C., Nocquet, J.-M., Walpersdorf, A., &
535 Castelltort, S. (2019). Present-day uplift of the European Alps: Evaluating mechanisms and
536 models of their relative contributions. *Earth-Science Reviews*, *190*, 589-604.

537 Stuhne, G. R., & Peltier, W. R. (2015). Reconciling the ICE-6G_C reconstruction of glacial
538 chronology with ice sheet dynamics: The cases of Greenland and Antarctica. *Journal of*
539 *Geophysical Research: Earth Surface*, *120*(9), 1841-1865.

540 Sue, C., Delacou, B., Champagnac, J. D., Allanic, C., & Burkhard, M. (2007). Aseismic
541 deformation in the Alps: GPS vs. seismic strain quantification. *Terra Nova*, *19*(3), 182-188.

542 Thorndycraft, V. R., Bendle, J. M., Benito, G., Davies, B. J., Sancho, C., Palmer, A. P.,
543 Fabel, D., Medialdea, A., & Martin, J. R. (2019). Glacial lake evolution and Atlantic-Pacific
544 drainage reversals during deglaciation of the Patagonian Ice Sheet. *Quaternary Science*
545 *Reviews*, *203*, 102-127.

546 Turcotte, D. L., & Schubert, G. (2002). *Geodynamics*. Cambridge university press.

547 van der Wal, W., Whitehouse, P. L., & Schrama, E. J. (2015). Effect of GIA models with 3D
548 composite mantle viscosity on GRACE mass balance estimates for Antarctica. Earth and
549 Planetary Science Letters, 414, 134-143.

550 Walpersdorf, A., Sue, C., Baize, S., Cotte, N., Bascou, P., Beauval, C., Collard, P, Daniel, G.,
551 Dyer, H., Grasso, J.-R., Hautecoeur, O., Helmstetter, A., Hok, S., Langlais, M., Menard, G.,
552 Mousavi, Z., Ponton, F., Rizza, M., Rolland, L., Souami, D., & Martinod, J. (2015).
553 Coherence between geodetic and seismic deformation in a context of slow tectonic activity
554 (SW Alps, France). *Journal of Geodynamics*, *85*, 58-65.

555 Watts, A. B. (2001). *Isostasy and Flexure of the Lithosphere*. Cambridge University Press.

556 Willis, M. J., Melkonian, A. K., Pritchard, M. E., & Rivera, A. (2012). Ice loss from the
557 Southern Patagonian ice field, South America, between 2000 and 2012. *Geophysical research*
558 *letters*, *39*(17).
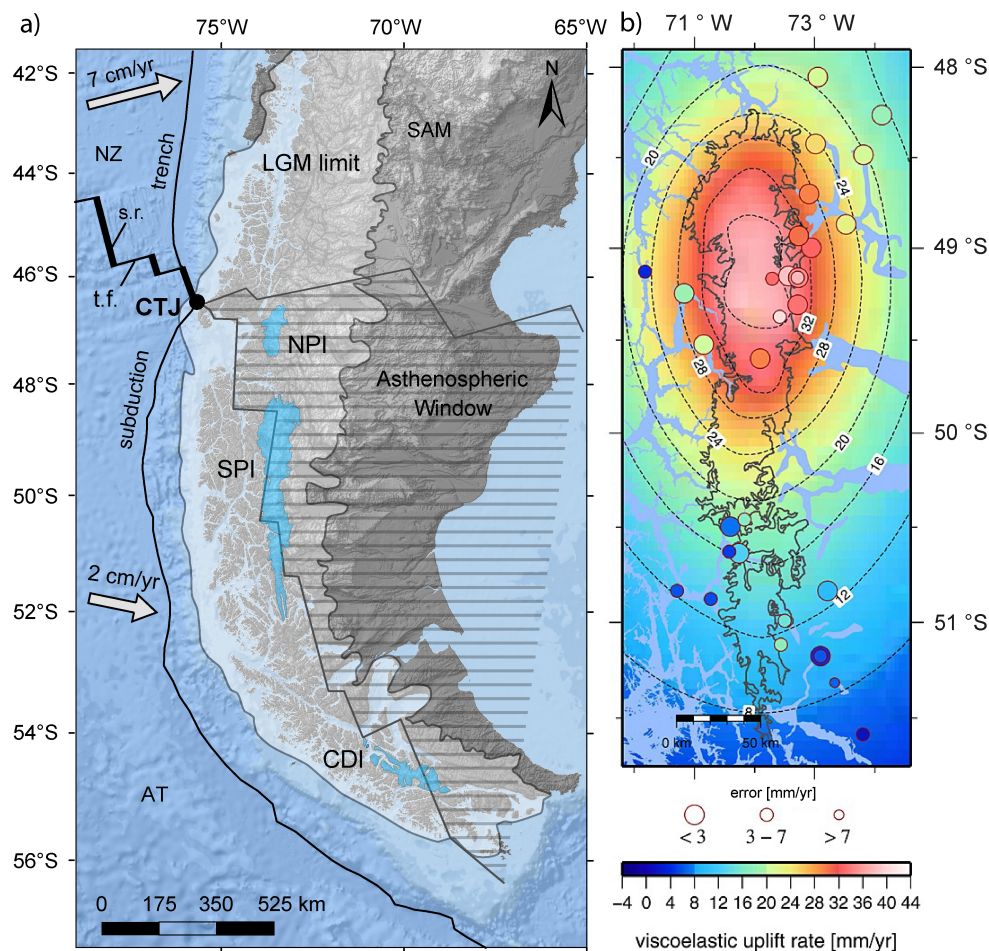
Fig. 1. Regional context and uplift rate data. a) Map of southern Patagonia with the Southern Patagonian Icefield (SPI), Northern Patagonian Icefield (NPI), and the Cordillera Darwin Icefield (CDI) in light blue, the approximate extension of the icefields at the Last Glacial Maximum (LGM limit), and the approximate extension of the present-day asthenospheric window (dashed region) beneath the South American Continent (SAM). In the Pacific Ocean, the spreading ridges (s.r., thick black lines) and transform faults (t.f., thin black lines) separate the Nazca (NZ) and the Antarctic (AT) plates. The subduction trench is also highlighted in black. The arrows show the approximate rate and direction of subduction of the oceanic plates. b) Zoom on the SPI with GPS stations (circles) used to estimate the viscoelastic uplift rates, from Lange et al. (2014).
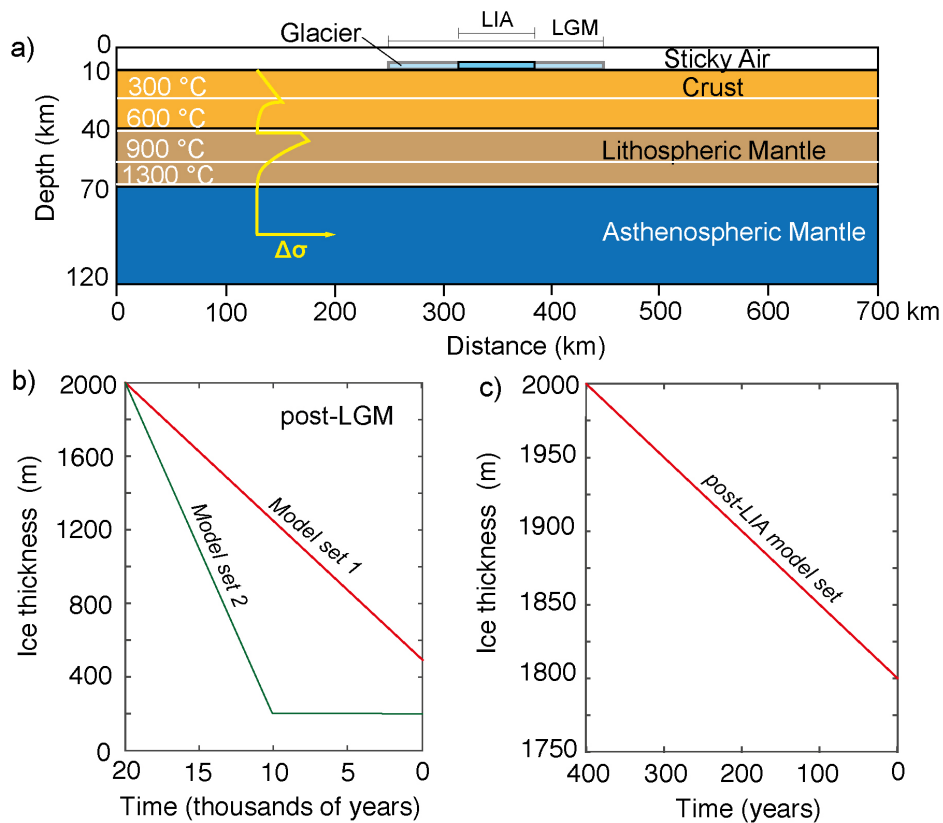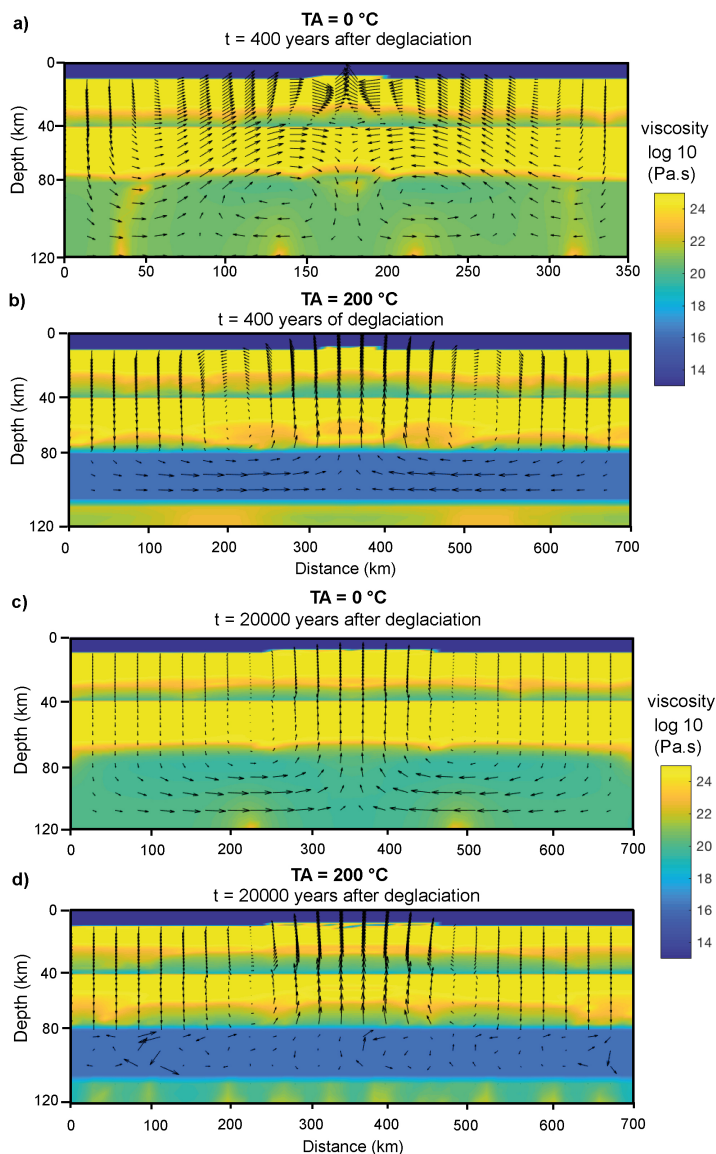
Fig. 2. Reference numerical model setup. a) Thermo-mechanical numerical model domain with rheological layers (Table 1), isotherms (white lines), and yield strength ($\Delta\sigma$) profile (yellow line). (b, c) Ice thickness vs. time used in the numerical models to simulate the post-LGM deglaciation in two model sets (b), and the post-LIA deglaciation (c).

570

18

Fig. 3. Distribution of viscosity and velocity vectors in the numerical models. a) Reference model without an asthenospheric thermal anomaly, TA = 0 °C, and b) model with the higher simulated asthenospheric thermal anomaly, TA = 200 °C, in the last timestep of post-LIA deglaciation. c) Reference model with TA = 0 °C, and d) model with TA = 200 °C, in the last timestep of *Model set 1* of post-LGM deglaciation. Velocity vectors do not have the same scaling and are only meant for visualization purpose.
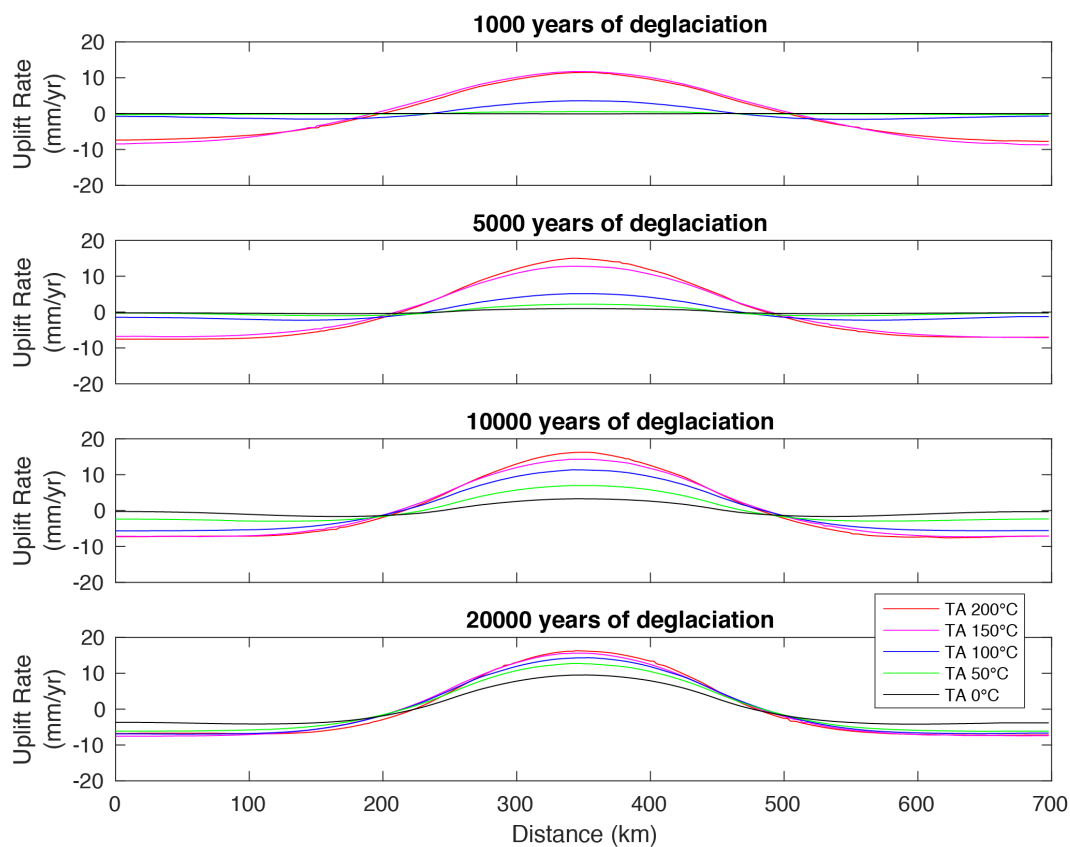
Fig. 4. Surface uplift rates vs. distance for *Model set 1* of post-LGM deglaciation. a) t = 1000 years of deglaciation, b) t = 5000 years of deglaciation, c) t = 10000 of deglaciation, d) 20000 years of deglaciation. Different line colours correspond to different TA.

580

20

Fig. 5. Surface uplift rates vs. distance for *Model set 2* of post-LGM deglaciation. a) t = 1000 years of deglaciation, b) t = 5000 years of deglaciation, c) t = 10000 of deglaciation, d) 20000 years of deglaciation. Different line colours correspond to different TA.
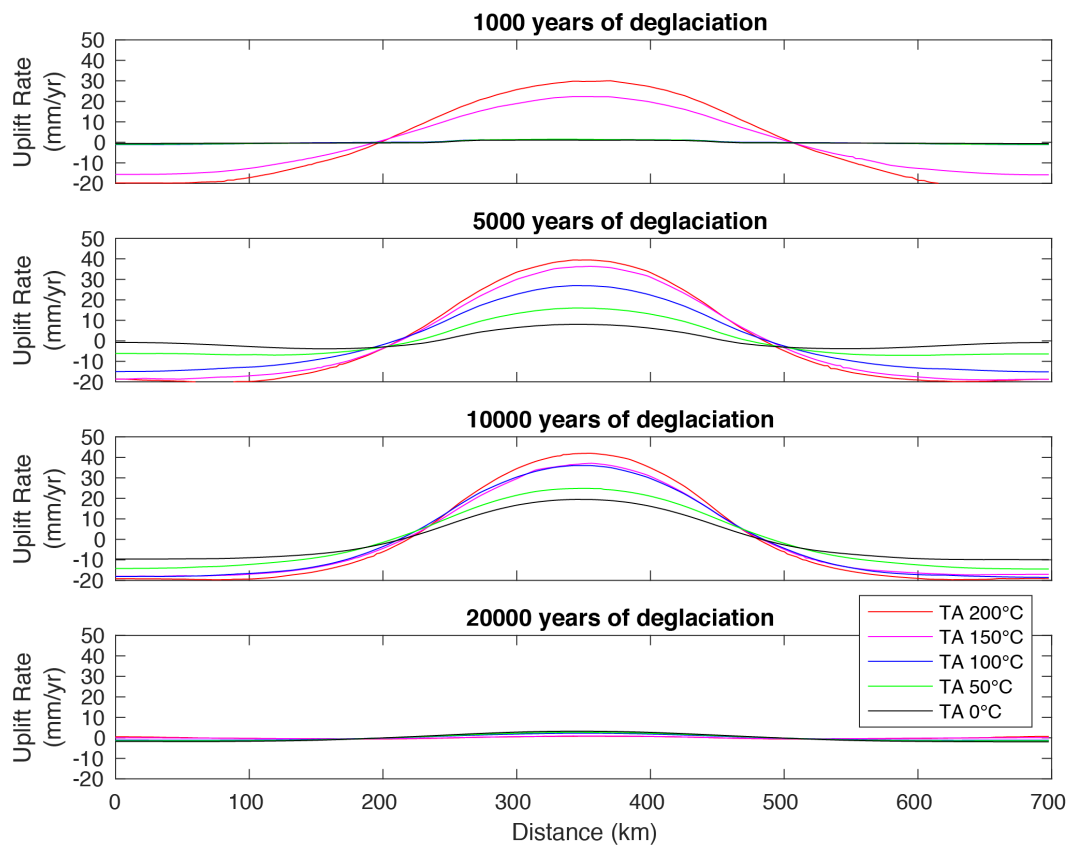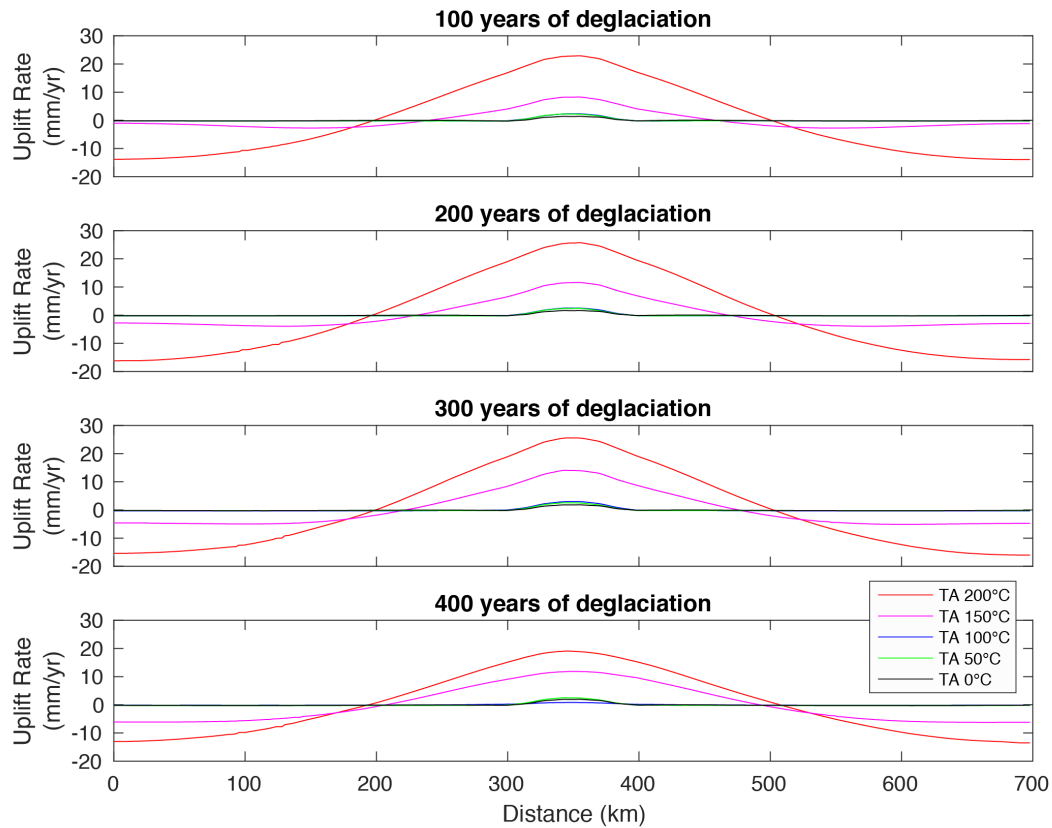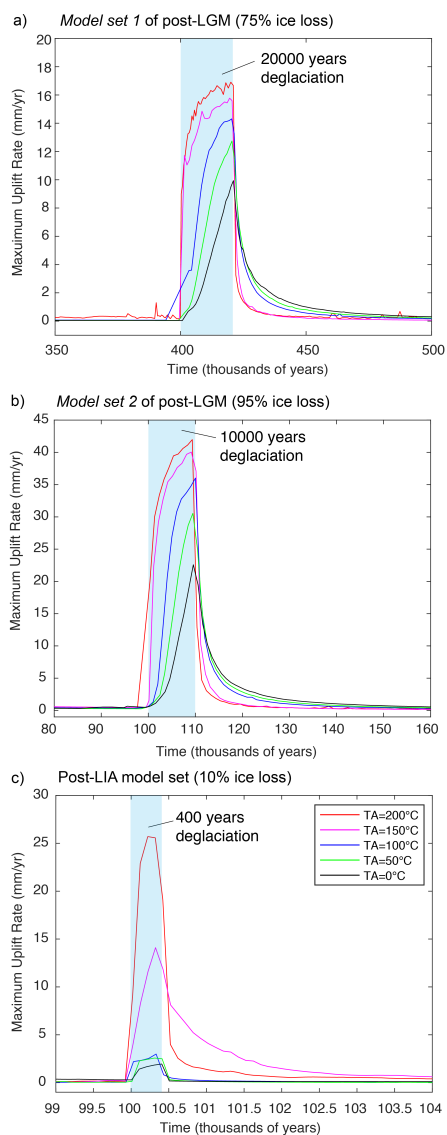
585

Fig. 6. Surface uplift rates vs. distance for post-LIA deglaciation model set. a) t = 100 years of deglaciation, b) t = 200 years of deglaciation, c) t = 300 years of deglaciation, d) 400 years of deglaciation. Different line colours correspond to different TA.

Fig. 7. Maximum uplift rates vs. time for model sets of deglaciation with different TA. a) *Model set 1* of post-LGM deglaciation accounting of 75% of ice loss in 20000 years, b) *Model set 2* of post-LGM deglaciation accounting of 95% of ice loss in 10000 years, and c) Post-LIA deglaciation model set accounting 10% of ice loss in 400 years (blue-shaded region). Blue-shaded regions highlight the modeled deglaciation intervals.

23

Table 1 – Material properties used in the numerical experiments.

	ρ_0^s (km/m^3)	E_a (kJ/mol)	V_a (m^3/mol)	n	C (MPa)	Visc. flow law	Sin (ϕ_{eff})	c (W/m/K)	μ (Gpa)	C_p (J/kg/K)	Hr (μW/m^3)	H_l (kJ/kg)	α (1/k)	β (1/Pa)
Crust	2800	154	0	2.3	10	Wet Qz.	0.2	0.64+807/(T+77)	10	1000	1	300	3x10^{-5}	1x10^{-11}
Lithos-pheric mantle	3250	532	10	3.5	10	Dry Ol.	0.6	0.73+1293/(T+77)	67	1000	0.022	400	3x10^{-5}	1x10^{-11}
Asthenos-pheric mantle	3250	532	10	3.5	10	Dry Ol.	0.6	0.73+1293/(T+77)	67	1000	0.022	400	3x10^{-5}	1x10^{-11}
Ice	920	154	0	2.3	10		0	0.73+1293/(T+77)	67	1000	0.022	400	3x10^{-5}	1x10^{-11}

595   ρ_0^s is the standard densities of solid rocks; E_a is the activation energy; V_a is the activation volume; n is the stress exponent; C is cohesion; φ_{eff} is the effective internal friction angle; c is thermal conductivity; μ is the shear modulus; C_p is the specific heat capacity; H_r and H_l are the radiogenic and latent heat productions, respectively; α is thermal expansion; β is compressibility. Qz and Ol are quartzite and olivine, respectively. All rheological and partial melting laws/parameters are based on experimental rock mechanics and petrology (Ranalli, 1995; Hirschmann, 2000; Johannes, 1985; Turcotte and Schubert, 2002).

600

Table 2 – Maximum uplift rates derived from the numerical models with a thermal anomaly (TA) of 0, 50, 100, 150 and 200 °C for the _Model set 1_ (a) and _Model set 2_ (b) of post-LGM deglaciation, and the post-LIA deglaciation model set (c). The t = 0 is the timestep immediately before the beginning of deglaciation. Fig. 7 is a plot of the maximum uplift rate vs. time calculated for each timestep in all numerical models.

a) _Model set 1_ of post-LGM deglaciation (20000 years)						
TA (°C)	Maximum uplift rate (mm/yr)					
0	0.0425	0.0412	0.9781	3.2849	6.4337	9.5049	4.9781
50	0.0481	0.5650	2.2171	6.9983	10.7568	12.7473	4.6591
100	0.0674	3.5812	5.1450	11.3702	13.6265	14.3080	4.0696
150	0.0471	11.7188	12.7860	14.3219	15.1838	15.5924	1.3896
200	0.1513	11.4839	15.0235	16.2639	16.4590	16.2576	0.8946
	t = 0	t = 1000 yr	t = 5000 yr	t = 10000 yr	t = 15000 yr	t = 20000 yr	t = 25000 yr

b) _Model set 2_ of post-LGM deglaciation (10000 years)						
TA (°C)	Maximum uplift rate (mm/yr)					
0	0.5011	1.0885	8.0324	19.4849	5.6972	3.1222	2.1536
50	0.2527	1.5170	15.9284	24.8744	5.2380	2.7184	1.7310
100	0.3270	1.2905	26.9424	36.0223	4.9357	2.3015	1.4085
150	0.4273	22.3004	36.3278	37.1107	1.9319	0.9322	0.5953
200	0.3725	30.0494	39.4609	41.9771	1.4801	0.7525	0.4868
	t = 0	t = 1000 yr	t = 5000 yr	t = 10000 yr	t = 15000 yr	t = 20000 yr	t = 25000 yr

c) post-LIA deglaciation model set (400 years)						
TA (°C)	Maximum uplift rate (mm/yr)					
0	0.4317	1.4151	1.6660	1.8366	1.9492	0.1764	0.1025
50	0.0352	2.2776	2.4264	2.5706	2.4514	0.3044	0.2340
100	0.0350	2.2024	2.3235	2.5241	2.9878	0.4854	0.3775
150	0.0933	8.2708	11.5730	14.0325	11.8261	8.1148	7.1503
200	0.0962	22.8938	25.7002	25.572	18.9666	3.9966	2.5535
	t = 0	t = 100 yr	t = 200 yr	t = 300 yr	t = 400 yr	t = 500 yr	t = 600 yr

605

25